Atmospheric Boundary Layer Height: Inter-Comparison of Different Estimation Approaches Using the Raman Lidar as Benchmark

Donato Summa [1,2], Gemine Vivone [1], Noemi Franco [2], Giuseppe D'Amico [1], Benedetto De Rosa [1,2] and Paolo Di Girolamo [2,*]

1. National Research Council-Institute of Methodologies for Environmental Analysis (CNR-IMAA), 85050 Tito, Italy
2. Scuola di Ingegneria, Università degli Studi della Basilicata, 85100 Potenza, Italy
* Correspondence: paolo.digirolamo@unibas.it

Abstract: This work stems from the idea of improving the capability to measure the atmospheric boundary layer height (ABLH) in variable or unstable weather conditions or in the presence of turbulence and precipitation events. A new approach based on the use of rotational and roto-vibrational Raman lidar signals is considered and tested. The traditional gradient approach based on the elastic signals at wavelength 532 nm is also considered. Lidar data collected by the University of Basilicata Raman lidar (BASIL) within the Special Observation Period 1 (SOP 1) in Cardillargues (Ceveninnes–CV supersite) during the Hydrological Cycle in the Mediterranean Experiment (HyMeX) were used. Our attention was specifically focused on the data collected during the period 16–21 October 2012. ABLH estimates from the Raman lidar were compared against other innovative methods, such as the recently established Morphological Image Processing Approach (MIPA) and the temperature gradient technique applied to potential temperature obtained from radio-sounding data. For each considered methodology, a statistical analysis was carried out. In general, the results from the different methodologies are in good agreement. Some deviations have been observed in correspondence with quite unstable weather conditions.

Keywords: atmospheric boundary layer; water vapor; aerosol; range corrected signals; MIPA; potential temperature; lidar; remote sensing

1. Introduction

The atmospheric boundary layer (ABL) is the region of the atmosphere directly in contact with the Earth's surface. The ABL undergoes complex interactions with the Earth's surface, the oceans, and the free troposphere. The timescale of the ABL response to surface forcing mechanisms is about 1 h [1]. Our limited comprehension and forecast capability of air pollution and extreme weather events, such as severe storms, are partially attributable to knowledge gaps in the processes taking place in the ABL. In fact, the ABLH defines the portion of the atmosphere undergoing strong vertical mixing and affected by pollutant dispersion, among others [2], and it is highly dependent on sea surface or land characteristics, atmospheric patterns, and solar heating. The ABLH is also an important variable in climate change modeling [3].

In the last few years, different approaches have been proposed to measure the ABLH, relying on the aerosol property of acting as tracers within the ABL [4,5] and considering that the elastic backscatter lidar signals are strongly dependent on the aerosol loading. One approach is based on the computation of the derivative of the elastic lidar backscatter signal [6–10]; alternative approaches consider the elastic backscatter lidar signal variance or a threshold signal level [11–17]. Another effective approach to estimate the ABLH relies on the application of a Haar wavelet covariance transform to elastic backscatter

lidar signals [18–20]. However, the application of the above-mentioned methodologies to the elastic backscatter lidar signals may produce false ABLH estimates in the presence of advection and local accumulation processes. This occurs especially if aerosol stratifications are present within the ABL [21].

ABL height and structure are difficult to characterize in complex and highly variable meteorological conditions. This issue has been tackled by several authors based on the use of multi-sensor data. The determination of the ABLH in cloudy conditions is characterized by possible interferences from cloud layers [22]. Machine learning methods have been proposed to estimate ABLH from elastic lidar data under complex weather conditions [23], with results revealing a sensitive reduction in the potential biases affecting ABLH estimates [24]. In general, the combined use of more sensors and approaches is preferred, especially in unstable weather conditions [25].

Additionally, the morphological image processing approach (MIPA) has been considered. MIPA is applied to high resolution elastic lidar signal time series and was already verified and validated in the frame of the European aerosol research lidar network (EARLINET), where the algorithm was applied considering a fully image-based methodology. One of the strengths of MIPA is its ability to deal with statistically significant time series of the whole attenuated backscatter profiles without exploiting profile-based processing as for traditional lidar ABLH retrievals. In this way, lidar data time correlation is considered to estimate ABLH as an additional parameter. The retrieval consists of applying a morphological operator and an edge detector to the composite image during the pre-processing phase. The post-processing phase includes the extraction of the significant edges through an object-based analysis. This latter has been demonstrated to be particularly suited for the determination of the ABLH.

In the present research effort, ABLH estimates obtained through the application of the MIPA are compared with those obtained through a new methodology based on the application of the derivative (gradient) to the pure rotational Raman lidar signals (mainly from nitrogen and oxygen molecules) and to roto-vibrational Raman lidar signals from water vapor molecules. Additionally, ABLH estimates from a wind profiler and those obtained from the application of the gradient approach to the range-corrected elastic backscatter signals at a wavelength of 532 nm are also considered. Finally, ABLH estimates obtained through the application of the temperature gradient approach to potential temperature profiles measured by the on-site radiosondes are taken as a reference.

The different approaches considered in the paper refer to different physical interpretations and, consequently, different atmospheric processes and variables. More specifically, the temperature gradient approach [26] applied to the potential temperature profiles from the on-site radiosondes is taken as a reference. This approach refers to the fact that sensible heat is transported in the ABL up to its top and, consequently, temperature gradients can be used to identify the ABLH.

ABLH estimates from the wind profiler rely on the turbulence method, which identifies the ABLH as the depth of the lowest continuous turbulence layer, where the turbulent region is determined by tracking the fluctuations of the different wind components measured by the wind profiler. Two additional approaches that have been considered are those based on the identification of gradients in the Raman lidar measurements, specifically in the temperature-sensitive rotational Raman signal profiles and in the water vapor mixing ratio profile measurements. The former of these two approaches relies on the temperature gradients found at the top of the ABL. The latter is instead based on the analogous water vapor mixing ratio gradients found at this height. Finally, the MIPA exploits the aerosol backscatter gradients and, consequently, the aerosol loading gradients found at the top of the ABL.

Lidar data considered in this paper are those collected by the Raman lidar BASIL. BASIL operated for a three-month period (September–November 2012) in Cardillargues (Ceveninnes–CV supersite) during the Hydrological Cycle in the Mediterranean Exper-

iment (HyMeX-SOP1). The period selected for the present inter-comparison effort was 16–21 October 2012, which was mostly affected by orographic rain.

The campaign HyMeX was conceived with the aim of improving our capability to predict high-impact weather events in the Mediterranean basin, based on an improved understanding of the hydrological cycle in this area. The orography surrounding the Mediterranean Sea favors atmospheric instability conditions in the region, which may trigger convection and, ultimately, lead to heavy precipitation events. Most of these events occur during the late summer or autumn, primarily in the western portion of the Mediterranean basin, with warm water acting as a heat source and humidity feeding convective systems.

The measurement period considered in this paper is characterized by highly variable meteorological conditions, which result in both aerosols and water contents visible as layers at different altitudes in BASIL observations. The characterization of the ABL height and structure in such complex weather conditions is particularly difficult and, in general, subjected to large uncertainties. On the other hand, the complexity of the measurement period is particularly suited for testing the performance of different ABLH retrieval algorithms.

The importance of assessing the performance of different ABLH retrieval algorithms against reference (radiosonde) values is to characterize the ABLH evolution with a finer temporal resolution. Since radiosonde launches are quite expensive, typically they are not available with enough time frequency to guarantee the study of the ABLH evolution on a small time scale. Differently, the alternative (with respect to the radiosondes) ABLH retrievals considered in this work have the advantage of allowing, in principle, a continuous monitoring (in time) of the ABLH as they are based on sensors capable of measuring in a continuous way. In general, advanced Raman lidars and wind profilers are expensive remote sensors. However, the implementation of one or both sensors in a network counting on several stations comparable to those present in the upper air network would certainly lead to a sensitive reduction in the costs.

The paper is organized as follows: Section 2 is dedicated to the illustration of the different approaches to estimating the ABLH. In Section 3, results obtained through these different approaches are reported and compared. Finally, conclusions are drawn in Section 4.

2. Dataset and Methodology

2.1. Raman Lidar BASIL

BASIL is a ground-based Raman lidar system developed around a Nd:YAG laser. The second and third harmonic generation modules allow the generation of laser pulses at 355, 532, and 1064 nm. The 355 nm wavelength is emitted to stimulate atmospheric Raman scattering processes. Water vapor and molecular nitrogen roto-vibrational Raman echoes are collected along with pure-rotational Raman echoes from nitrogen and oxygen molecules. These lidar echoes allow us to measure water vapor mixing ratios [27,28] and atmospheric temperature [29,30] profiles. Single-pulse energy at 355 nm is found to be 500 mJ, which corresponds to 10 W at 20 Hz. The receiver includes a 0.45 m diameter Newtonian telescope and two small lenses (diameter = 0.05 m) dedicated to collecting the 532 and 1064 nm elastic backscatter echoes. High-resolution and accurate profile measurements of atmospheric temperature and humidity are carried out by BASIL both during the daytime and at nighttime through the rotational and roto-vibrational Raman lidar techniques, respectively [31–35]. BASIL also provides particle backscattering coefficient profiles at 355, 532, and 1064 nm, particle extinction coefficient profiles at 355 and 532 nm, and particle depolarization ratio profiles at 355 and 532 nm [36–39].

During HyMeX-SOP1, BASIL was at the Ceveninnes–Vivres observational site (Candillargues, Lat: 43°37′N, Lon: 4°04′E, Elevation: 1 m) and operated in an almost continuous way during the period 5 September–5 November 2012.

2.2. ABLH Estimates Obtained from the Elastic Backscatter, Pure-Rotational, and Roto-Vibrational Raman Lidar Signal Gradients

ABLH estimates can be obtained through a well-consolidated approach relying on the sensitivity of elastic backscatter echoes to suspended particles' concentration and its variability. Aerosols, being more abundant within the ABL than in the free troposphere, can act as tracers of atmospheric motions. Specifically, elastic backscatter lidar signals at 532 nm, which are used in the present paper to estimate the ABLH, are strongly dependent on the atmospheric aerosol loading and its gradients, and consequently, they can be used to estimate the ABLH as the top of the first (from the surface) detected aerosol layer. To deal with quantities proportional to the atmospheric aerosol backscatter, the lidar signals have been expressed in terms of range-corrected signals (RCSs). The use of this quantity also allows us to remove from the elastic backscatter signals the noise components associated with solar background and detector noise. RCS at 532 nm, hereafter indicated as $RCS_{532}(z)$, is defined as:

$$RCS_{532}(z) = \left[P_{\lambda_{532}}(z) - P_{bgd} \right] z^2 \tag{1}$$

where $P_{\lambda_{532}}(z)$ represents the elastic backscatter lidar signal at 532 nm from altitude z and P_{bgd} represents the solar background and the detector noise.

According to what has already been mentioned, the ABLH can be determined as the altitude at which the first significant gradient of the RCS occurs. Such a method is known as the "derivative approach" and has been used for years within the lidar community. The novelty we discuss in the present paper is the application of the same methodology to a pure N_2 and O_2 rotational Raman signal and to the water vapor mixing ratio measured by BASIL lidar.

Rotational Raman signals from nitrogen and oxygen molecules are strongly dependent on atmospheric temperature and its variability. In this respect, it is recalled that ABLH estimates are traditionally inferred by identifying local maxima in the gradient of potential temperature profiles. So far, this approach has been primarily applied to meteorological radiosonde data. In this study, we also evaluate its applicability to the temperature-sensitive rotational Raman lidar signals in the UV.

The approach can also be applied to the power ratio of two rotational Raman signals with opposite temperature sensitivity. In this regard, it is specified that rotational Raman lines from nitrogen and oxygen molecules are present in the proximity of the laser wavelength, λ_0. More specifically, rotational lines closer to λ_0, characterized by small values of the rotational quantum number, J, tend to increase in intensity when temperature decreases, while the opposite behavior is observed in rotational lines characterized by large values of J, whose intensity increases when temperature increases. Lidar signals generated by rotational Raman lines from nitrogen and oxygen molecules with opposite temperature behavior can be collected within two narrow spectral regions located close to λ_0, which can be indicated as $P_{LoJ}(z)$ and $P_{HiJ}(z)$. BASIL operates with a UV laser wavelength at $\lambda_0 = 354.7$ nm and includes two narrow interferential filters centered at $\lambda_{LoJ} = 354.3$ nm (low quantum number filter) and at $\lambda_{HiJ} = 352.9$ nm (high quantum number filter) [40].

Estimates of the ABLH are obtained as the minimum of the derivative of the natural logarithm of the signal ratio $P_{HiJ}(z)/P_{LoJ}(z)$. Thus, we have:

$$ABLH = min\left\{ \frac{d}{dz} \left[ln\left(\frac{P_{HiJ}(z)}{P_{LoJ}(z)} \right) \right] \right\}. \tag{2}$$

The availability of a water vapor Raman channel in BASIL allows us to test another approach to obtain the ABLH. Roto-vibrational Raman lidar signals from water vapor and nitrogen molecules, $P_{H2O}(z)$ and $P_{N2}(z)$, respectively, can be used to determine the vertical profile of the atmospheric water vapor mixing ratio, $\chi_{H2O}(z)$, through the expression:

$$\chi_{H2O}(z) = K \frac{P_{H2O}(z) T_{N2}(z)}{P_{N2}(z) T_{H2O}(z)} \tag{3}$$

where $T_{N2}(z)$ and $T_{H2O}(z)$ are the atmospheric transmissivity at the roto-vibrational Raman shifted wavelength for nitrogen and water vapor molecules, respectively, and K is a calibration constant that can be determined through an independent measurement typically carried out by radiosondes, GPS, or microwave radiometers. Water vapor mixing ratio is an atmospheric quantity preserved in dynamic and thermodynamic processes taking place within the boundary layer when condensation processes are not taking place (that is in most cloud-free conditions). Consequently, water vapor can be used as an additional tracing parameter of atmospheric motion, with the atmospheric water vapor mixing ratio gradients possibly being used to infer the ABLH. Note that the gradients of the water vapor mixing ratio are independent from the calibration constant K, which is needed only to compute the absolute values of the water vapor mixing ratio. In the present paper, we infer the ABLH from the water vapor signals by applying a derivative approach to the logarithm of $\chi_{H2O}(z)$, thus identifying the minimum of the gradient. To reduce signal statistical fluctuations and to allow the application of the derivative approach, an integration time of 5 min is considered both during the daytime and night-time measurements. Moreover, to further improve the signal-to-noise ratio, a vertical smoothing with a vertical window of 150 m is also applied to the raw data, which has a raw resolution of 30 m. Of course, an approach similar to this will only work if there is enough water vapor in the atmosphere to act as an ABL tracer. Consequently, such a methodology is not indicated for studying the ABL in dry conditions. Typically, lidar signals are characterized by a quite high signal-to-noise ratio at the altitudes where the ABLH is usually observed. A provisional evaluation of this uncertainty has been given in [41], with a value comparable to the raw vertical resolution of the data (i.e., 30 m). Therefore, the ABLH uncertainty due to lidar-signal statistical fluctuation [42] is negligible. Raman lidar is a very powerful and straightforward technique to measure water vapor mixing ratio profiles, especially during nighttime conditions. The performance is somewhat degraded during daytime because of the small Raman cross-sections, reducing the covered vertical range to 4–5 km [43,44]. However, as will be illustrated below, signal degradation does not seem to affect the correct applicability of the derivative approach applied to $\chi_{H2O}(z)$.

2.3. MIPA-WCT Techniques

This section gives an overview of the state-of-the-art morphological image processing approach (MIPA) [45] used to infer the ABLH from lidar observations. More specifically, in this study, an image obtained as a sequence of consecutive elastic range-corrected signals at 532 nm calculated according to (1) is considered. MIPA consists of four main blocks:

(1) A vertical resolution adjustment step to reach a (target) working spatial resolution (around 20 m).
(2) A pre-processing based on mathematical morphology.
(3) An edge detector i.e., a wavelet covariance transform (WCT).
(4) A post-processing algorithm, which, by relying on both mathematical morphology and object-based analysis, allows us to obtain the result. It is worth noting that MIPA is a blind approach and, thus, does not exploit any prior information. Specific details about the four blocks of the MIPA framework are provided below:

- The vertical spatial resolution adjustment block starts from a matrix I: E ⊆ Z2 → V ⊆ Z, which is the daily sequence of the $RCS_{532}(z)$ profiles forming the columns of **I**. The down-sampling with a factor **R**, aimed to reduce the bins' spatial resolution, is implemented by a low-pass filter (i.e., a moving-average filter) along each column of **I** plus decimation with a factor **R**. This latter is a tuning parameter selected to have a spatial resolution not finer than 20 m (implying that for data with a spatial resolution coarser than 20 m, this step is skipped). The outcome is denoted as $\mathbf{I}_D$.
- A low-pass filter based on half-gradients is used to pre-process $\mathbf{I}_D$. A line-structuring element in the horizontal direction (i.e., the time direction) is exploited, thus smoothing the lidar image along the horizontal axis (where the

dynamic of the ABL is expected to be quite slow), reducing noise, and preserving vertical edges. The result of the preprocessing of $\mathbf{I}_D$ is denoted as $\mathbf{I}_{pre}$.

- Every edge detector can generally be exploited to extract a first estimation of the ABLH starting from $\mathbf{I}_{pre}$ (e.g., the WCT, Canny's edge detector, or a gradient-based approach). In this work, we make use of a WCT to obtain a first estimate of the edge map, $\mathbf{E}$. The detected edges in $\mathbf{E}$ are indicated with 1, while the rest of the map (background) is labeled as 0. All bins labeled as 1 in the edge map are potential candidates to represent the ABLH.

- The edge map, $\mathbf{E}$, is further analyzed through post-processing procedures. More specifically, morphological filters are exploited first to remove unrealistic edges (i.e., edges that are too fast with respect to the dynamics of the ABL). Hence, a series of directional low-pass morphological filters [46] are applied, varying the related angles and combining the outputs with a maximum operator. Finally, object-based processing is applied to the result obtained by the application of the morphological filtering. The main idea behind this latter approach is the use of the connectivity (i.e., the way in which the bins labeled as "edge", which assume value 1, are spatially-related to their neighbors) in the edge map to form objects. An analysis of the spatial variability of these objects is then performed. Indeed, if the absolute Euclidean distance between the means of the heights for each extracted object and the related means calculated on the objects in its neighborhood exceeds a predefined threshold value, this object is removed from the solution. The estimated ABLH, denoted as $\mathbf{E}_{out}$, is obtained by linearly interpolating the remaining objects in the edge map (for further details, see Algorithm 1).

Algorithm 1 The steps of the MIPA framework

---

1 Vertical spatial resolution adjustment of $\mathbf{I}$ by a factor R to obtain $\mathbf{I}_D$

---

2 Pre-process $\mathbf{I}_D$ by low-pass filtering using half-gradients to obtain $\mathbf{I}_{pre}$

---

3 Detection of the edges of $\mathbf{I}_{pre}$ using the WCT to obtain the edge map $\mathbf{E}$

---

4 Post-process $\mathbf{E}$ using directional morphological filters and an object-based analysis to obtain $\mathbf{E}_{out}$

2.4. WIND Profiler Radar (WPR)

A detailed description of the WPR and its main working parameters, data processing methodologies, and delivered geophysical products is given in [47]. The methodology to determine the ABLH is based on the identification of a strong, distinctive peak in the WPR time-height reflectivity plot. However, a strong uncertainty in the ABLH measurement derives from the false peaks associated with temperature and humidity gradients and with the presence of insect swarms [48].

2.5. Temperature Gradient Method

The temperature gradient method identifies inversions in the potential temperature profile, which are often present at the ABL top. The potential temperature, $\theta(z)$, is given by the expression:

$$\theta(z) = T(z) \left(\frac{P_0}{P(z)} \right)^{\gamma} \tag{4}$$

where P_0 is the surface normal pressure (1013 hPa), $T(z)$ and $P(z)$ are the atmospheric pressure and temperature profiles, respectively, and γ is equal to 0.286 for air.

The potential temperature is nearly constant within a well-mixed layer. Maximum values of the potential temperature vertical gradient identify the transition from a convectively unstable to a stable vertical region. Stable layers may inhibit turbulent eddies and the development of deep convection.

In this work, the temperature gradient method is applied to the data measured by radiosondes launched from the lidar site, and the corresponding ABLH estimates are considered a reference.

A radiosonde launching facility was installed in early September 2012 in the proximity of the lidar station in the frame of HyMeX-SOP1. Launched radiosondes, manufactured by Vaisala (model: RS92), rely on a thin-wire temperature sensor characterized by a very fast response time and equipped with a hydrophobic coating for protection to reduce the effects of evaporative cooling after emerging from clouds. About twenty radiosonde launches were made within the selected measurement period (generally every 6 h starting from 16 October at 23:00). All available radiosonde data on site (about twenty) was linearly interpolated with a time resolution of 5 min and used as references for the calculation of the absolute and relative bias affecting the other techniques [49,50]. Table 1 summarizes all the instruments and also the techniques used to determine ABLH, with the corresponding pros and cons.

Table 1. Summary of the considered instruments/approaches used to determine the ABLH.

Instruments	Techniques Details	Approaches
Radiosondes RS	*Pros*: Input: Potential temperature profile obtained by measured atmospheric pressure and temperature. High accuracy and high spatial resolution of the data. Launch time was generally every 6 h (starting from 16 October at 00:00) on the 16–21 October dataset. *Cons*: Low time resolution; expensive.	Gradient method applied on $\theta(z)$ These values are used as reference
Lidar	*Pros*: High spatial and temporal resolution of pure rotational Raman profiles *Cons*: In some cases, low signal-to-noise ratio (SNR) may reduce sensitivity; require smoothing; no measurement with rain.	Rotational (Rot) Derivative of Ratio $[H_{ij}(z)/L_{oj}(z)]$
	Pros: High spatial and temporal resolution of roto-vibrational Raman profiles (water vapour, nitrogen) *Cons*: In some cases, low signal-to-noise ratio (SNR) may reduce sensitivity; require smoothing; no measurement with rain. Not accurate in dry conditions.	Water Vapor (WV) Derivative of Ratio $[H_2O(z)/N_2(z)]$
	Pros: High resolution time series (in both space and time) of elastic lidar RCS 532 nm *Cons*: No measurement with rain.	MIPA ABLH determination by using WCT edge detection
WPR	*Pros*: High temporal sampling, all weather condition measurements *Cons*: UHF signals sensitivity to birds and clutter, reducing the detectability of atmospheric signals on one or more of the off-vertical beams; multiple peaks in SNR with a consequent attribution problem; precipitations can influence the accuracy of wind measurements depending on intensity and duration of precipitation.	UHF band with a primary frequency at 1.274 GHz ABLH determination relies on the identification of a distinctive strong peak in the WPR time-height reflectivity plot

3. Results

Figure 1a reports the time series of the RCS at 532 nm as measured by BASIL with a time resolution of 5 min and a vertical resolution of 30 m. The evolution of the water vapor mixing ratio over the same period considered in Figure 1a is shown in Figure 1b.
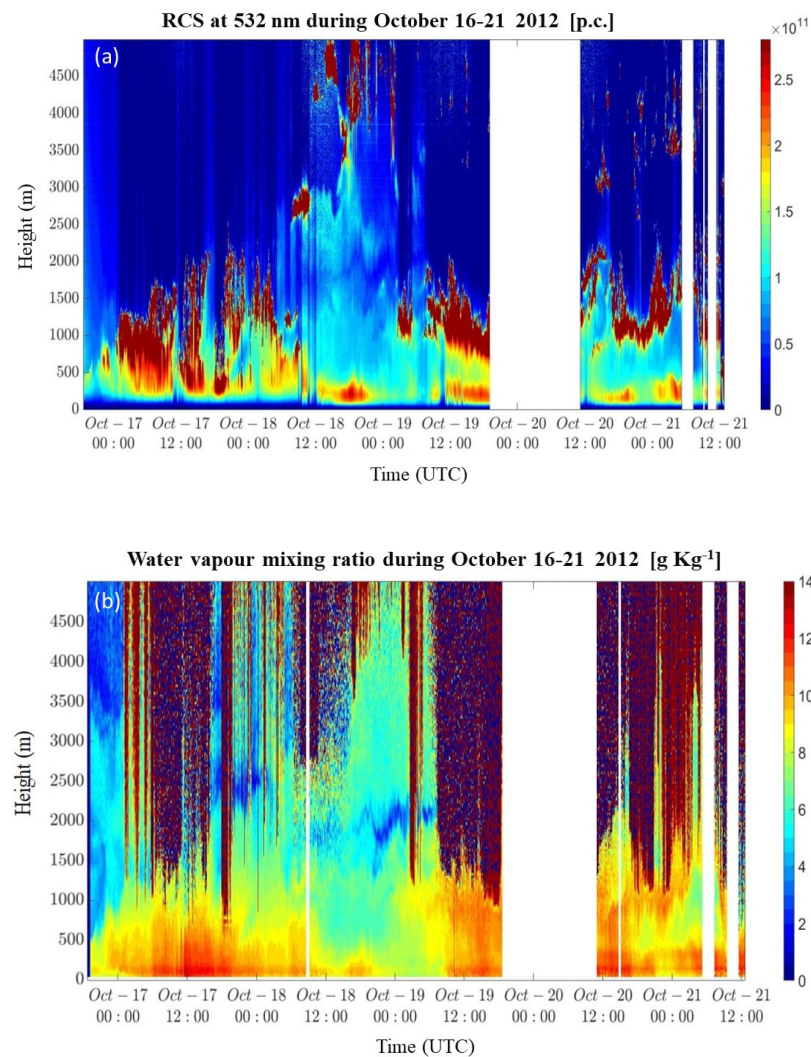
Figure 1. Time-height cross-section of the RCS at 532 nm (**a**) measured by Raman lidar BASIL and (**b**) water vapor mixing ratio over Cardillargues during 16–21 October 2012.

Both the figures reveal the complex aerosol and cloud structure occurring during the period under consideration (16–21 October 2022), which is characterized by highly variable meteorological conditions. More specifically, several aerosol and humidity layers are present at different altitudes, as well as water and mixed-phase clouds. The characterization of the ABL height in such complex weather conditions is particularly challenging and, in general, is affected by large uncertainties. In previous studies from the same and other authors, it was demonstrated that the characterization of the ABLH can be effectively pursued by combining observations made by different sensors and different methodological retrieval approaches. The weather conditions occurring during the considered measurement period result from the deepening of a large low-pressure system over Spain and Portugal and the associated cold front. A low-altitude flow is present over the Mediterranean Sea, which brings warm, humid air and persistent orographic rainfall events to the CV area. On 19 October, the isolated low-pressure system in the southern part of the elongated depression area near Portugal began moving northeast from Morocco to Murcia. An event of high rainfall hit eastern Spain on that day [51].

RCS measurements on 17 October (Figure 1a) indicate the presence of a mesoscale convective system, with convective clouds visible between 0.5 and 2 km. Precipitations beneath these clouds are observed at 11:00 UTC and from 17:00 to 19:00 UTC. The shading effect of the clouds prevented the onset of convection during the daylight portion of the day, which ultimately translated into a limited ABL growth clearly visible in Figure 1a.

On 18 October, lidar observations show the presence of broken clouds at about 1.2–1.5 km during nighttime and more stable weather conditions starting from 12:00 UTC with an ABLH gradually decreasing below 0.5 km due to the reduced solar activity. Above the ABL, other aerosol layers and mixed-phase clouds are observed at about 4.5 km. Moreover, Figure 1b reveals the coexistence of an aerosol and a humid layer both in the ABL and above, one extending from the ground up to about 2 km and another one from 2 km up to the cloud base at 4.5 km. The separation of two layers at 2 km is visible in both the RCS (Figure 1a) and water vapor (Figure 1b) plots. Stratiform clouds on 19 October show a descending cloud base from 1.4 to 0.8 km.

The measurements corresponding to the last observational period (starting from 20 October 12:00 UTC) show a well-developed ABL in the first part, with convective clouds forming at its top. During the following hours, both the RCS and water vapor plots indicate the formation of two layers: one below 600–700 m (presumably the ABL) and another one above, just below the cloud bottom.

These complex weather conditions are well suited to test the different sensors/models/approaches and their performance. As already specified above, different approaches have been considered for the determination of the ABLH. In all the cases, ABLH estimates come from signal profiles with a vertical and time resolution of 30 m and 5 min, respectively. Figure 2 illustrates the evolution of the ABLH estimated through the different approaches. In general, the overall agreement is good, with an increasing trend of the ABLH until the central part of the day on 18 October, an abrupt decrease during the second part of the same day and the morning of 19 October, an abrupt new increase during the central part of the day on 19 October, and a final progressive decrease late on 20–21 October. The abrupt increase revealed through all the compared approaches on 19 October is most probably due to a sudden increase in the main motor friction coefficient of the ABL [52–54].
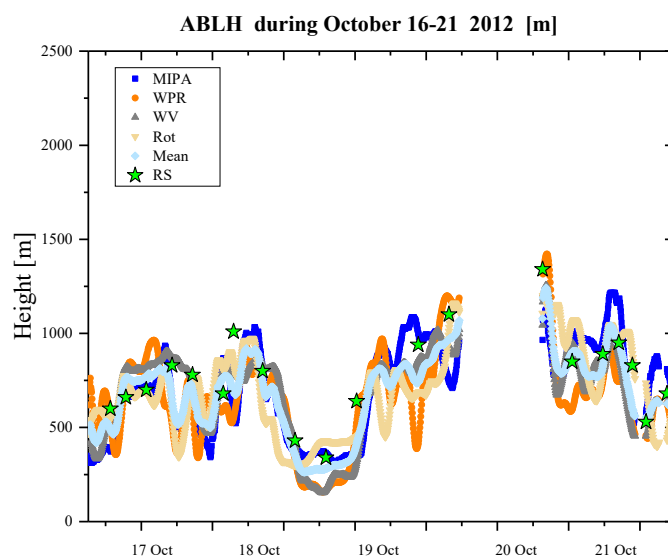
Figure 2. Comparison of ABLH estimated using different methods with reference values obtained from the temperature gradient technique applied to on-site radiosonde data (green stars) during the period from 16–21 October 2012.

Table 2 reports the relative biases between the ABLH estimates from the different approaches and those obtained with the reference approach. Relative biases with respect to reference are expressed in terms of minima (i.e., min), maxima (i.e., max), average, and standard deviation (i.e., σ). Moreover, a linear fitting of the different approaches versus reference is also provided. These statistical parameters have been calculated for the whole dataset (i.e., from 16 to 21 October). Moreover, four different sub-intervals have been considered for calculating the average of the relative biases for each sub-interval. These subintervals have been selected to highlight differences in terms of ABLH retrieval perfor-

mance under stable and unstable conditions. More specifically, we selected two strongly unstable periods (16–17 October and 20–21 October) characterized by very low (and potentially precipitating) clouds and two more stable periods (18 October and 19 October) in which the clouds are located at higher altitudes.

Table 2. Statistical analysis, considering relative biases, of the ABLH estimates obtained with the different approaches/sensors. The linear fitting ($Y = A \cdot X$) of the compared approaches versus radiosondes (on site) is also reported.

Approaches	MIPA (%)	Rot (%)	WPR (%)	WV(%)	Mean of Approaches (%)	
Average	−2.28	−7.99	−4.57	−4.60	−4.79	
Max	39.10	23.08	21.29	30.23	13.74	
Min	−38.06	−38.60	−31.94	−38.09	−25.57	
σ	15.98	14.05	12.73	12.29	9.66	
Linear Fitting ($Y = A \cdot X$)						
A	0.87	0.90	0.85	0.90	0.89	
s(A)	0.036	0.032	0.04	0.032	0.024	
R^2	0.94	0.95	0.92	0.95	0.97	
Days						*Weather Conditions*
16–17 Oct	−11.24	−6.70	−8.06	−7.24	−4.31	Unstable
18 Oct	−7.86	−8.09	−7.76	−3.71	−6.61	Stable
19 Oct	4.08	3.70	−4.55	2.30	−1.35	Stable
20–21 Oct	12.89	7.72	−9.98	4.52	1.42	Unstable

Values reported in Table 2 are also illustrated in Figures 3 and 4, where the relative bias (%) and scatter plot of all the compared approaches against radiosondes are reported. These figures clearly reveal that MIPA, which is the only approach based uniquely on RCSs, provides effective ABLH estimates in the time interval 18–20 October 2012, with a mutual bias with respect to the reference of 4–8% in correspondence of the two selected stable sub-intervals, while larger deviations are found on 16–17 and 21 October 2012 (unstable conditions), with values as large as −11.24% and +12.89%, respectively. The approaches that seem to be more accurate during stable conditions are those based on the application of the derivative algorithm to $\chi_{H2O}(z)$ and to the logarithm of the rotational signal ratio $P_{HiJ}(z)/P_{LoJ}(z)$, with relative bias values smaller than 7.24% and 7.72%, respectively. A possible explanation for such behavior could be the enhanced aerosol deposition (within the ABL) occurring under unstable weather conditions. The lower aerosol concentration in the ABL could explain the larger deviations produced by MIPA, which is the only algorithm working on the elastic RCS. The water vapor content is expected to be less affected by deposition processes, while the methodology based on the pure rotational Raman signals is not affected at all because it works on molecular targets.

The wind profiler is found to generally underestimate the ABLH. However, estimates from different sensors/approaches are in good agreement, with the correlation coefficient always in the range of 0.92 to 0.97. The mean ABLH estimate obtained by averaging estimates from all the sensors/approaches is characterized by a smaller relative bias (values not exceeding 4.3%). This outcome highlights the benefit of combining ABLH estimates obtained through different sensors and methodologies.
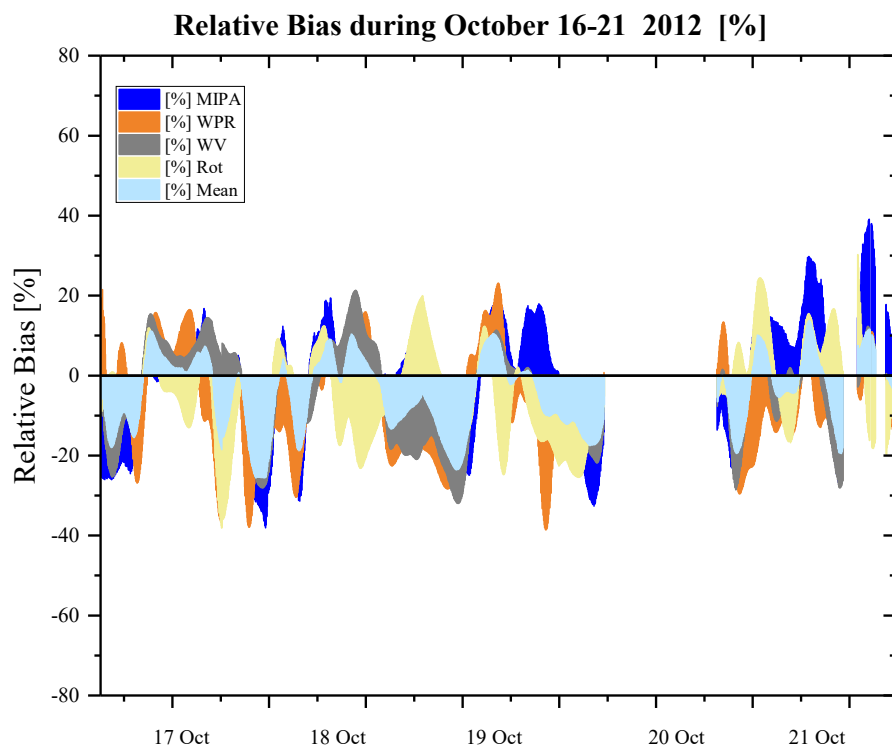
Figure 3. Relative biases (%) of the ABLH estimates obtained by the compared methods with respect to reference data during the period 16–21 October 2012.
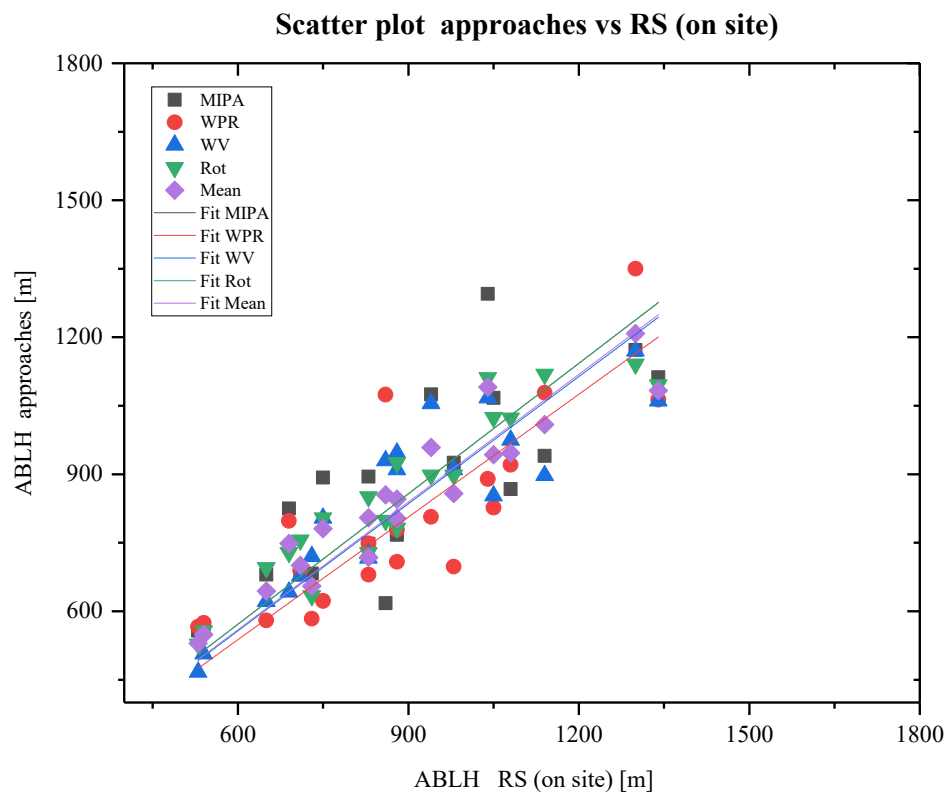
Figure 4. Comparison of different ABLH estimates expressed in terms of linear fitting for each approach. The *x*-axis shows the ABLH reference values obtained by applying the potential temperature approach to in-situ radiosondes, while the *y*-axis refers to the estimates provided by the compared approaches.

4. Conclusions

Different approaches to estimating the ABLH have been applied to the measurements collected by BASIL Raman Lidar during the period 16–21 October 2012, in the frame of HyMeX-SOP 1. This measurement period is characterized by highly variable meteorological conditions, which result in the presence of stratified aerosol and water vapor features at different altitudes. Several approaches have been considered, including some very innovative ones, such as the temperature-dependent pure rotational signals collected by the Raman lidar systems BASIL and MIPA. Additionally, a novel methodology to obtain an estimation of the ABLH from the lidar-retrieved water vapor mixing ratio profile has been investigated. Moreover, other approaches have been considered, such as the one based on the identification of a peak in the WPR time-height reflectivity plot and the gradient methodology applied to potential temperature profiles measured by radiosondes.

Even though the ABLH retrieved from radiosondes is considered accurate, the limited number of launches typically available, even during intensive observation periods, often does not allow an accurate characterization of the ABLH time evolution. However, different sensors/approaches, probing the atmosphere continuously, can fill this gap by providing high-resolution ABLH estimates in both time and space. Some of these approaches were proposed and tested in the present research effort, where lidar data with a vertical resolution of 30 m and a time resolution of 5 min have been used as input to obtain the ABLH. Results reveal a generally good agreement among the ABLH estimates from the different sensors/approaches (relative bias always smaller than 12.89%). The ABLH estimate based on the application of the gradient approach to the potential temperature profiles from the on-site radiosondes was used as a reference. Under unstable weather conditions (high relative humidity and low clouds), the approaches that appear to be more accurate are those based on the derivative technique applied to the logarithms of $\chi_{H2O}(z)$ and $P_{HiJ}(z)/P_{LoJ}(z)$, with relative biases with respect to the reference smaller than -7.24% and -8.09%, respectively. Results also reveal that the mean ABLH estimate obtained by averaging ABLH retrievals from all the approaches is characterized by the smallest relative bias with respect to the reference (values not exceeding 4.3%), which underlines the benefit of combining different sensors/approaches, especially in complex weather conditions.

Author Contributions: D.S., G.V., N.F., G.D., B.D.R. and P.D.G. collaborated and contributed to drafting, reviewing and editing the paper. In particular, P.D.G. and D.S. coordinated the effort and wrote the original draft. G.V., N.F., G.D. and B.D.R. contributed to the reviewing of the data analysis algorithms and final text, the data analysis and the paper All authors have read and agreed to the published version of the manuscript.

Funding: This research has been supported by the French National Research Agency (ANR) (grant nos. MISTRALS/HyMeX and ANR-11-BS56-0005 IODA-MED project), the Italian Ministry for Education, University and Research (grants STAC-UP and FISR2019-CONCERNING), and the Italian Space Agency (grants As-ATLAS and CALIGOLA).

Data Availability Statement: The data considered in the paper are accessible through the following repositories: https://www.hymex.org/ (last access: 25 July 2021; HyMeX, 2021) and https://www.ncei.noaa.gov/products/weather-balloon/ integrated-global-radiosonde-archive (last access: 16 June 2021; NOAA NCEI, 2021).

Acknowledgments: We wish to thank Said Frèdèrique, from Laboratoire d'Aérologie, Université de Toulouse, for the provision of the wind profiler data. This research effort was funded by the Italian Ministry for University and Research (Grant FISR2019-CONCERNING) and by the Italian Space Agency (Grants: As-ATLAS and CALIGOLA).

Conflicts of Interest: The authors declare no conflict of interest.

References

1. Stull, R.B. An introduction to boundary layer meteorology (Volume 13). In *Springer Science & Business Media*; Springer: Berlin/Heidelberg, Germany, 1998; Volume 13.
2. Melfi, S.H.; Spinhirne, J.D.; Chou, S.H.; Palm, S.P. Lidar observations of vertically organized convection in the planetary boundary layer over the ocean. *J. Appl. Meteorol. Climatol.* **1985**, *24*, 806–821. [CrossRef]
3. Flamant, C.; Pelon, J.; Flamant, P.H.; Durand, P. Lidar determination of the entrainment zone thickness at the top of the unstable marine atmospheric boundary layer. *Bound.-Layer Meteorol.* **1997**, *83*, 247–284. [CrossRef]
4. Di Girolamo, P.; Ambrico, P.F.; Amodeo, A.; Boselli, A.; Pappalardo, G.; Spinelli, N. Aerosol observations by lidar in the nocturnal boundary layer. *Appl. Opt.* **1997**, *38*, 4585–4595. [CrossRef] [PubMed]
5. Summa, D.; Di Girolamo, P.; Flamant, C.; De Rosa, B.; Cacciani, M.; Stelitano, D. Water vapour inter-comparison effort in the framework of the hydrological cycle in the Mediterranean experiment—Special observation period (hymex-sop1). *EPJ Web Conf.* **2018**, *176*, 08016. [CrossRef]
6. Russell, P.B.; Uthe, E.E.; Ludwig, F.L.; Shaw, N.A. A comparison of atmospheric structure as observed with monostatic acoustic sounder and lidar techniques. *J. Geophys. Res.* **1974**, *79*, 5555–5566. [CrossRef]
7. Menut, L.; Flamant, C.; Pelon, J.; Flamant, P.H. Urban boundary-layer height determination from lidar measurements over the Paris area. *Appl. Opt.* **1999**, *38*, 945–954. [CrossRef]
8. Bösenberg, J.; Linné, H. Laser remote sensing of the planetary boundary layer. *Meteorol. Z.* **2002**, *11*, 233–240. [CrossRef]
9. Frioud, M.; Mitev, V.; Matthey, R.; Haoeberli, C.; Richner, H.; Werner, R.; Vogt, S. Backscatter lidar observation of the aerosol stratification over Rhine Valley during a heat wave in September 1999. In Proceedings of the Remote Sensing of Clouds and the Atmosphere VII, Honolulu, HI, USA, 24–26 September 2018; International Society for Optics and Photonics: Bellingham, DC, USA, 2003; Volume 4882, pp. 420–431.
10. Matthias, V.; Balis, D.; Bösenberg, J.; Eixmann, R.; Iarlori, M.; Komguem, L.; Wang, X. Vertical aerosol distribution over Europe: Statistical analysis of Raman lidar data from 10 European Aerosol Research Lidar Network (EARLINET) stations. *J. Geophys. Res. Atmos.* **2004**, *109*, 1–5. [CrossRef]
11. Pal, S.; Behrendt, A.; Wulfmeyer, V. Elastic-backscatter-lidar-based characterization of the convective boundary layer and investigation of related statistics. *Ann. Geophys.* **2010**, *28*, 825–847. [CrossRef]
12. Hayden, K.L.; Anlauf, K.G.; Hoff, R.M.; Strapp, J.W.; Bottenheim, J.W.; Wiebe, H.A.; McKendry, I.G. The vertical chemical and meteorological structure of the boundary layer in the Lower Fraser Valley during Pacific'93. *Atmos. Environ.* **1997**, *31*, 2089–2105. [CrossRef]
13. Steyn, D.G.; Baldi, M.; Hoff, R.M. The detection of mixed layer depth and entrainment zone thickness from lidar backscatter profiles. *J. Atmos. Ocean. Technol.* **1999**, *16*, 953–959. [CrossRef]
14. Hoff, R.M.; Harwood, M.; Sheppard, A.; Froude, F.; Martin, J.B.; Strapp, W. Use of airborne lidar to determine aerosol sources and movement in the Lower Fraser Valley (LFV), BC. *Atmos. Environ.* **1997**, *31*, 2123–2134. [CrossRef]
15. Hägeli, P.; Steyn, D.G.; Strawbridge, K.B. Spatial and temporal variability of mixed-layer depth and entrainment zone thickness. *Bound. Layer Meteorol.* **2000**, *97*, 47–71. [CrossRef]
16. Cohn, S.A.; Angevine, W.M. Boundary layer height and entrainment zone thickness measured by lidars and wind-profiling radars. *J. Appl. Meteorol.* **2000**, *39*, 1233–1247. [CrossRef]
17. Brooks, I.M. Finding boundary layer top: Application of a wavelet covariance transform to lidar backscatter profiles. *J. Atmos. Ocean. Technol.* **2003**, *20*, 1092–1105. [CrossRef]
18. Morille, Y.; Haeffelin, M.; Drobinski, P.; Pelon, J. STRAT: An automated algorithm to retrieve the vertical structure of the atmosphere from single channel lidar data. *J. Atmos. Ocean. Technol.* **2007**, *24*, 761–775. [CrossRef]
19. Di Girolamo, P.; De Rosa, B.; Summa, D.; Franco, N.; Veselovskii, I. Measurements of aerosol size and microphysical properties: A comparison between Raman lidar and airborne sensors. *J. Geophys. Res. Atmos.* **2022**, *127*, e2021JD036086. [CrossRef]
20. Behrendt, A.; Pal, S.; Aoshima, F.; Bender, M.; Blyth, A.; Corsmeier, U.; Wulfmeyer, V. Observation of convection initiation processes with a suite of state-of-the-art research instruments during COPS IOP 8b. *Q. J. R. Meteorol. Soc.* **2011**, *137*, 81–100. [CrossRef]
21. Haeffelin, M.; Angelini, F.; Morille, Y.; Martucci, G.; Frey, S.; Gobbi, G.P.; Feist, D.G. Evaluation of mixing-height retrievals from automatic profiling lidars and ceilometers in view of future integrated networks in Europe. *Bound. Layer Meteorol.* **2012**, *143*, 49–75. [CrossRef]
22. Dang, R.; Yang, Y.; Li, H.; Hu, X.-M.; Wang, Z.; Huang, Z.; Zhou, T.; Zhang, T. Atmosphere Boundary Layer Height (ABLH) Determination under Multiple-Layer Conditions Using Micro-Pulse Lidar. *Remote Sens.* **2019**, *11*, 263. [CrossRef]
23. Liu, Z.; Chang, J.; Li, H.; Chen, S.; Dai, T. Estimating Boundary Layer Height from LiDAR Dataunder Complex Atmospheric Conditions Using Machine Learning. *Remote Sens.* **2022**, *14*, 418. [CrossRef]
24. Dang, R.; Yang, Y.; Hu, X.-M.; Wang, Z.; Zhang, S.A. Review of Techniques for Diagnosing the Atmospheric Boundary Layer Height (ABLH) Using Aerosol Lidar Data. *Remote Sens.* **2019**, *11*, 1590. [CrossRef]
25. Joffre, S.M.; Kangas, M.; Heikinheimo, M.; Kitaigorodskii, S.A. Variability of the stable and unstable atmospheric boundary layer height and its scales over a boreal forest. *Bound. Lay. Meteorol.* **2001**, *99*, 429–450. [CrossRef]
26. Bianco, L.; Wilczak, J.M. Convective boundary layer depth: Improved measurement by Doppler radar wind profiler using fuzzy logic methods. *J. Atmos. Ocean. Technol.* **2002**, *19*, 1745–1758. [CrossRef]

27. Whiteman, D.N.; Melfi, S.H.; Ferrare, R.A. Raman lidar system for the measurement of water vapor and aerosols in the Earth's atmosphere. *Appl. Opt.* **1992**, *31*, 3068–3082. [CrossRef] [PubMed]

28. Di Girolamo, P.; Flamant, C.; Cacciani, M.; Richard, E.; Ducrocq, V.; Summa, D.; Saïd, F. Observation of low-level wind reversals in the Gulf of Lion area and their impact on the water vapour variability. *Q. J. R. Meteorol. Soc.* **2016**, *142*, 153–172. [CrossRef]

29. Di Girolamo, P.; Scoccione, A.; Cacciani, M.; Summa, D.; Rosa, B.D.; Schween, J.H. Clear-air lidar dark band. *Atmos. Chem. Phys.* **2018**, *18*, 4885–4896. [CrossRef]

30. Behrendt, A.; Reichardt, J. Atmospheric temperature profiling in the presence of clouds with a pure rotational Raman lidar by use of an interference-filter-based polychromator. *Appl. Opt.* **2000**, *39*, 1372–1378. [CrossRef]

31. Di Girolamo, P.; Marchese, R.; Whiteman, D.N.; Demoz, B.B. Rotational Raman Lidar measurements of atmospheric temperature in the UV. *Geophys. Res. Lett.* **2004**, *31*, 1–5. [CrossRef]

32. Di Girolamo, P.; Summa, D.; Ferretti, R. Multiparameter Raman lidar measurements for the characterization of a dry stratospheric intrusion event. *J. Atmos. Ocean. Technol.* **2009**, *26*, 1742–1762. [CrossRef]

33. Di Girolamo, P.D.; Summa, D.; Lin, R.F.; Maestri, T.; Rizzi, R.; Masiello, G. UV Raman lidar measurements of relative humidity for the characterization of cirrus cloud microphysical properties. *Atmos. Chem. Phys.* **2009**, *9*, 8799–8811. [CrossRef]

34. Di Girolamo, P.D.; Cacciani, M.; Summa, D.; Scoccione, A.; Rosa, B.D.; Behrendt, A.; Wulfmeyer, V. Characterisation of boundary layer turbulent processes by the Raman lidar BASIL in the frame of HD (CP) 2 Observational Prototype Experiment. *Atmos. Chem. Phys.* **2017**, *17*, 745–767. [CrossRef]

35. De Rosa, B.D.; Girolamo, P.D.; Summa, D. Temperature and water vapour measurements in the framework of the Network for the Detection of Atmospheric Composition Change (NDACC). *Atmos. Meas. Tech.* **2020**, *13*, 405–427. [CrossRef]

36. Di Girolamo, P.; Summa, D.; Bhawar, R.; Di Iorio, T.; Cacciani, M.; Veselovskii, I.; Kolgotin, A. Raman lidar observations of a Saharan dust outbreak event: Characterization of the dust optical properties and determination of particle size and microphysical parameters. *Atmos. Environ.* **2012**, *50*, 66–78. [CrossRef]

37. Di Girolamo, P.; Summa, D.; Cacciani, M.; Norton, E.G.; Peters, G.; Dufournet, Y. Lidar and radar measurements of the melting layer: Observations of dark and bright band phenomena. *Atmos. Chem. Phys.* **2012**, *12*, 4143–4157. [CrossRef]

38. Di Girolamo, P.; De Rosa, B.; Flamant, C.; Summa, D.; Bousquet, O.; Chasette, P.; Totems, J.; Cacciani, M. Water vapor mixing ratio and temperature inter-comparison results in framework of the Hydrological Cycle in the Mediterranean Experiment Special Observation Period 1. *Bull. Atmos. Sci. Technol.* **2020**, *1*, 113–153. [CrossRef]

39. Martucci, G.; Matthey, R.; Mitev, V.; Richner, H. Frequency of boundary-layer-top fluctuations in convective and stable conditions using laser remote sensing. *Bound. Layer Meteorol.* **2010**, *135*, 313–331. [CrossRef]

40. Summa, D.; Di Girolamo, P.; Stelitano, D.; Cacciani, M. Characterization of the planetary boundary layer height and structure by Raman lidar: Comparison of different approaches. *Atmos. Meas. Tech.* **2013**, *6*, 3515–3525. [CrossRef]

41. Summa, D.; Madonna, F.; Franco, N.; De Rosa, B.; Di Girolamo, P. Inter-comparison of atmospheric boundary layer (ABL) height estimates from different profiling sensors and models in the framework of HyMeX-SOP1. *Atmos. Meas. Tech.* **2022**, *15*, 4153–4170. [CrossRef]

42. Liu, F.; Wang, R.; Yi, F.; Huang, W.; Ban, C.; Pan, W.; Wang, Z.; Hu, H. Pure rotational lidar for full-day troposphere temperature measurement at Zhongshan Station (69.37°S, 76.37°E), Antarctica. *Optics Express.* **2021**, *29*, 10059–10076. [CrossRef] [PubMed]

43. Althausen, D.; Müller, D.; Ansmann, A.; Wandinger, U.; Hube, H.; Clauder, E.; Zörner, S. Scanning 6-wavelength 11-channel aerosol lidar. *J. Atmos. Ocean. Technol.* **2000**, *17*, 1469–1482. [CrossRef]

44. Whiteman, D.N.; Demoz, B.; Rush, K.; Schwemmer, G.; Gentry, B.; Di Girolamo, P.; Van Hove, T. Raman lidar measurements during the International H$_2$O Project. Part I: Instrumentation and analysis techniques. *J. Atmos. Ocean. Technol.* **2006**, *23*, 157–169. [CrossRef]

45. Vivone, G.; D'Amico, G.; Summa, D.; Lolli, S.; Amodeo, A.; Bortoli, D.; Pappalardo, G. Atmospheric boundary layer height estimation from aerosol lidar: A new approach based on morphological image processing techniques. *Atmos. Chem. Phys.* **2021**, *21*, 4249–4265. [CrossRef]

46. Soille, P. *Morphological Image Analysis: Principles and Applications*; Springer: Berlin/Heidelberg, Germany, 2003.

47. Gage, K.S.; Balsley, B.B.; Ecklund, W.L.; Woodman, R.F.; Avery, S.K. Wind-profiling Doppler radars for tropical atmospheric research. *Eos Trans. AGU* **1990**, *71*, 1851–1854. [CrossRef]

48. Saïd, F.; Campistron, B.; Delbarre, H.; Canut, G.; Doerenbecher, A.; Durand, P.; Legain, D. Offshore winds obtained from a network of wind-profiler radars during HyMeX. *Q. J. R. Meteorol. Soc.* **2016**, *142*, 23–42. [CrossRef]

49. Madonna, F.; Summa, D.; Di Girolamo, P.D.; Marra, F.; Wang, Y.; Rosoldi, M. Assessment of Trends and Uncertainties in the Atmospheric Boundary Layer Height Estimated Using Radiosounding Observations over Europe. *Atmosphere* **2021**, *12*, 301. [CrossRef]

50. Dirksen, R.J.; Sommer, M.; Immler, F.J.; Hurst, D.F.; Kivi, R.; Vömel, H. Reference quality upper-air measurements: GRUAN data processing for the Vaisala RS92 radiosonde. *Atmos. Meas. Tech.* **2014**, *7*, 4463–4490. [CrossRef]

51. Ducrocq, V.; Davolio, S.; Ferretti, R.; Flamant, C.; Santaner, V.H.; Kalthoff, N.; Richardh, E.; Heini Wernli, H. Introduction to the Hymex special issue on "Advanced in understanding and forecasting of heavy precipitation in the Mediterranean thought the Hymex SOP1 field campaign". *Q. J. R. Meteorol. Soc.* **2016**, *142* (Suppl. 1), 1–6. [CrossRef]

52. De Rosa, B.; Amato, F.; Amodeo, A.; D'Amico, G.; Dema, C.; Falconieri, A.; Mona, L. Characterization of Extremely Fresh Biomass Burning Aerosol by Means of Lidar Observations. *Remote Sens.* **2022**, *14*, 4984. [CrossRef]

53. Flamant, C.; Chazette, P.; Caumont, O.; Di Girolamo, P.; Behrendt, A.; Sicard, M.; Wulfmeyer, V. A network of water vapor Raman lidars for improving heavy precipitation forecasting in southern France: Introducing the WaLiNeAs initiative. *Bull. Atmos. Sci. Technol.* **2021**, *2*, 10. [CrossRef]

54. Chazette, P.; Flamant, C.; Raut, J.C.; Totems, J.; Shang, X. Tropical moisture enriched storm tracks over the Mediterranean and their link with intense rainfall in the Cevennes-Vivarais area during HyMeX. *Q. J. R. Meteorol. Soc.* **2016**, *142*, 320–334. [CrossRef]